19th Brazilian Congress of Thermal Sciences and Engineering
November 6th–10th, 2022, Bento Gonçalves - RS - Brazil

ENC-2022-0248
NUMERICAL STUDY OF A FREE-SURFACE LAMINAR FLOW OF A NON-NEWTONIAN FLUID OVER A FIXED SUBMERGED SOLID BODY

William Oliveira, williamoliveira0409@gmail.com
Guilherme Henrique Fiorot, guilherme.fiorot@ufrgs.br
Laboratório de Reologia e Escoamento de Fluidos Não Newtonianos - ReoSul, Universidade Federal do Rio Grande do Sul - UFRGS, Rua Sarmento Leite 425, Porto Alegre, RS, 90050-170.

Abstract. *Mass movements on steep slopes constitute risks and warnings regarding discussions of natural catastrophes. Since vulnerable regions can be violently hit, exposing human lives to danger, the search for preventive solutions is inevitable. In countries where hydrological and geological factors are present, integrating the morphological terrain aspect, mud and debris flow are examples of natural disasters. As such flow drags solid material and sediments, it is essential to know the relationship between the flow and a submerged solid body. Therefore, to understand this type of scenario, this work comprises the numerical study of a free-surface flow in an open channel presenting a bed slope angle. The fluid is non-Newtonian, viscoplastic, and approximated by the non-linear Herschel-Bulkley model. This work also evaluates an equivalent Newtonian fluid for identical boundary conditions. The computer simulation is performed in OpenFOAM, using the VOF model for the interface solution. This work initially evaluates the flow kinematics by studying the velocity and pressure fields. Then, it analyses the magnitude of the forces, drag and lift coefficients, acting on the solid body as a function of its characteristic dimension. The free-surface height evaluates the flow behavior according to its approximation with the solid body.*

Keywords: *Non-Newtonian fluid, CFD simulation using OpenFOAM, fixed solid body, Herschel-Bulkley, Volume of Fluid (VOF).*

1. INTRODUCTION

Mass movements are a type of geophysical flow that involves a water-sediment mixture. The literature classifies these fine-grained gravitational movements under different names in accord with the solid fraction and the material type: flood, solids transport, hyper-concentrated flows, mudflows, debris flows, granular flows, landslides, avalanches, etc. Different climates and terrain conditions can trigger these natural catastrophes occurring in mountainous areas (Berti *et al.*, 1999; Chen *et al.*, 2021; Mueting *et al.*, 2021). The impact of such phenomena can have disastrous effects because of their enormous destructive potential. Geophysical observations can be made from an event relating to its harmful nature: flood, soil detachment, and intense materials mobilization such as rocks of variable size and format. Arises then a necessity for estimating the flow properties through predictive models since communities and buildings located in vulnerable areas are extremely sensitive to those events. There are also extensive reporting occurrences of this type of event in Brazil, where hydrological and geological factors are dominant regarding the morphological terrain aspect (Cabral *et al.*, 2021; Gramani and Arduin, 2015; Kanji *et al.*, 2008). Figure 1 exemplifies these events and the consequences of sediment transport along the Serra do Mar, Brazil.

The general classification of mass movements is based on two parameters: the solid fraction and the material type. Among different types, debris flows are peculiar events in which a large volume of highly concentrated viscous water-debris mixture is transported. Then, two extreme forms of debris flow are distinguished: muddy debris flows and granular debris flows (Coussot and Meunier, 1996). For muddy debris flows, Malet *et al.* (2003) show the viscoplastic characteristic of this material, the shear-thinning behavior toward high shearing rates, and its representation by the Herschel-Bulkley model. Fluids with a small concentration of sediments retain their Newtonian properties (Ancey, 2007). However, it can show variation in its viscosity depending on the concentration (Maciel *et al.*, 2009). Therefore, understanding the relationship between Newtonian and non-Newtonian fluids is relevant because the latter complete classification depends on the solid fraction concentration.

The problem can be modeled as a free-surface flow on an infinitely wide inclined plane with an angled slope, two-dimensional, exclusively governed by the action of gravitational acceleration. In this work, a CFD model is developed

(a) Sediment transport in a ravine zone, Serra da Prata, Paraná.

(b) Channel bed after a debris flow event in the Guarda-Mão stream, São Paulo.

Figure 1: Mass movement occurrences at Serra do Mar, Brazil (Picanço *et al.*, 2019).

via OpenFOAM to represent such a mathematical problem. The simulation implements two types of fluid to predict and understand the flow behavior and its drag capacity: non-Newtonian, which is the objective brought by this present work, and Newtonian fluid, dynamic and kinematic equivalent to the previous one.

The solution evaluates a steady and uniform laminar flow, seeking to understand interactions between the flowing fluid and a structure represented by a submerged solid body. This work initially evaluates the flow kinematics and dynamics during various simulated scenarios by employing different geometric characteristics of the obstacle. Then, we assess the magnitude of acting forces on the solid body as a function of its characteristic dimension. Finally, the drag and lift coefficients are studied as a function of the submergence ratio of the obstacle. The free-surface height is also evaluated to see the flow behavior according to its approximation with the solid body.

2. METHODOLOGY

2.1 Geometry

The geometry corresponds to an open channel presenting a bed slope angle of θ, as shown in Fig. 2, that allows the fluid to proceed downhill. The flow has its surface in contact with the atmosphere, characterizing a free surface flow. The gravitational acceleration, g, is the driving force. The quota in the Cartesian coordinate system corresponds to y, while x is the abscissa. Having its origin on the left face of the solid body, the x^* is the auxiliary axis. The non-Newtonian rheological properties are the flow index n, the flow consistency K, and the yield stress τ_0. The density and the kinematic viscosity are ρ_m, and $\nu_{0,m}$, respectively. The Newtonian fluid parameters are the density ρ_N, the dynamic and kinematic viscosity represented respectively by μ and $\nu_{0,N}$. The fixed solid body structure is shown with its height H_{SB} and length L_{SB}. In the present study, the length of L_{SB} is maintained constant, while its height varies. The flow depth is $h_{0,m}$ for the non-Newtonian fluid, whereas for the Newtonian is $h_{0,N}$. Both relations $h_{0,m} > H_{SB}$ and $h_{0,N} > H_{SB}$ are always valid since the study concerns a submerged body. The subscript *m* corresponds to mud, while *N* is to the Newtonian fluid.

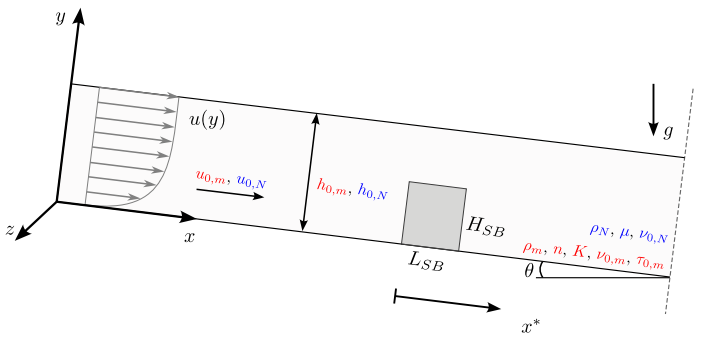

Figure 2: Steep slope and solid body diagrams, along with the kinematic, geometric, and rheological parameters for both non-Newtonian (red) and Newtonian (blue) fluids.

2.2 Mathematical methodology

The mathematical model arises to validate the numerical model and is divided into two principal procedures: the mathematical formulation of the problem regarding a non-Newtonian fluid and the sequencing to find an equivalent Newtonian fluid to the previous one.

2.2.1 Non-Newtonian fluid equations

The equations of motion are obtained from the Cauchy equations by neglecting the $O(\varepsilon^2)$ term and setting $\varepsilon = h/L$, where h is the total depth of flow and L is the characteristic length. Applying the simplifying hypothesis, the conservation equations for mass (Eq. 1) and *momentum* (Eq. 2) are presented:

$$\frac{\partial u}{\partial x} + \frac{\partial v}{\partial y} = 0 \tag{1}$$

$$\begin{aligned} \rho_m \left(\frac{\partial u}{\partial t} + u\frac{\partial u}{\partial x} + w\frac{\partial v}{\partial y} \right) &= -\frac{\partial P}{\partial x} + \rho_m g \sin\theta + \frac{\partial}{\partial y}(\tau_{xy,m}) \\ \frac{\partial P}{\partial y} &= -\rho_m g \cos\theta \end{aligned} \tag{2}$$

On both equations above, $\mathbf{U} = (u, v, 0)$ is the velocity vector, u is the longitudinal velocity, v is the vertical velocity, P is the pressure, and t is time. The term $\partial P/\partial y$ shows that the solution for P leads to a hydrostatic pressure. The stress $\tau_{xy,m}$ is conserved and properly described by an adequate rheological model. At the free surface, the boundary conditions are given by the kinematic condition as a function $y = h(x,t)$, at atmospheric pressure. The validation procedure of the rheological model follows the equations used by Irgens (2014) and Fiorot and Maciel (2019). The Herschel-Bulkley model describes the rheologic characteristic of the muddy fluid as shown in Eq. (3), expressed for simple shear conditions.

$$\tau_{xy,m} = \tau_0 + K\left(\frac{\partial u}{\partial y}\right)^n, \tag{3}$$

to $\tau_{xy,m} > \tau_0$, otherwise, $\partial u/\partial y = 0$. The shear rate is according to Eq. (4).

$$\dot{\gamma}_m = \frac{du}{dy} = \left(\frac{\rho_m g(h_{0,m} - y)\sin\theta - \tau_0}{K}\right)^{\frac{1}{n}} \tag{4}$$

The velocity profile is given by Eq. (5):

$$u(y) = \left(\frac{n}{n+1}\right)\left(\frac{\rho_m g y_0^{n+1}\sin\theta}{K}\right)^{\frac{1}{n}}\left[1 - \left(1 - \frac{y}{y_0}\right)^{\frac{1}{n}+1}\right] \tag{5}$$

The flow depth in the sheared region is given by Eq. (6):

$$y_0 = h_{0,m}(1 - C), \tag{6}$$

where C represents the dimensionless yield stress (Eq. (7)),

$$C = \frac{\tau_0}{\rho_m g h_{0,m}\sin\theta} \tag{7}$$

The plug velocity refers to the non-sheared region of the flow, that is, where the velocity profile is constant along the y-axis (Eq. (8)):

$$u_{y_0} = \left(\frac{n}{n+1}\right)\left(\frac{\rho_m g y_0^{n+1}\sin\theta}{K}\right)^{\frac{1}{n}} \tag{8}$$

The mean velocity is given by Eq. (9):

$$u_{0,m} = \left(\frac{n}{n+1}\right)\left(\frac{\rho_m g\sin\theta}{K} y^{n+1}\right)^{\frac{1}{n}}\left(\frac{1+n+nC}{2n+1}\right) \tag{9}$$

And finally, Eq. (10) presents the apparent viscosity for the non-Newtonian fluid.

$$\nu_{0,m} = \frac{\tau}{\rho_m \dot{\gamma}_m} = \frac{1}{\rho_m}\left(\frac{\tau_0}{\dot{\gamma}_m} + k\dot{\gamma}_m^{n-1}\right) \tag{10}$$

2.2.2 Dynamic equations

The imposed forces applied on the submerged body can be viscous (Eq. 11) or pressure (Eq. 12) forces:

$$F_v = \sum_m s_{f,m} \cdot \boldsymbol{R}_{dev} \tag{11}$$

$$F_p = \sum_m \rho_m s_{f,m} \left(p_m - p_{ref}\right) \tag{12}$$

where $\boldsymbol{R}_{dev}$ is the Deviatoric Stress Tensor[1].

In addition, related to the flow dynamics, the drag and lift coefficients are presented in Eq. (13) and Eq. (14), respectively, adapted from the literature Pritchard and Mitchell (2015):

$$C_D = \frac{F_D}{\frac{1}{2}\rho u_0^2 A_P} \tag{13}$$

$$C_L = \frac{F_L}{\frac{1}{2}\rho u_0^2 A_P} \tag{14}$$

In the two previous equations, F_D and F_L are equivalent, respectively, to the resulting forces acting on the x and y axes. The solid body projected area is A_P. The width of the obstacle is equivalent to the flow depth for each simulation.

2.3 Numerical methodology

The numerical simulation is performed in OpenFOAM, an open-source software written in C++ language and running on a Linux operating system, which employs around 250 predefined applications simulating physical cases related to fluid mechanics, combustion processes, thermodynamics, turbulence models, rheological models, chemical kinetics, and heat transfers, among others (OpenFOAM UserGuide, 2020).

The numerical solution is obtained via `interFoam` solver, an algorithm that is based on the Volume of Fluid (VOF) method used for the two-phase flow configuration of a biviscous Herschel-Bulkley fluid. The VOF method employs the species transport equation to determine a relative volume fraction of the two phases, or phase fraction α, in each computational cell. OpenFOAM solves the *momentum* and continuity equations in a complete three-dimensional form by default. However, it can be instructed to solve in two dimensions by specifying an empty boundary condition on boundaries normal to the z-direction, for which no solution is required.

The numerical validation is established by considering the non-Newtonian fluid. This procedure is desirable since this type of fluid is characterized by higher gradients and should therefore produce inaccuracy for simulation results. A numerical adaptation in Eq. (10) is necessary to resolve the existing discontinuity for the numerical resolution of a problem involving a non-Newtonian Herschel-Bulkley fluid. Nguyen *et al.* (2006) propose a bi-viscous model that introduces linearity in this discontinuity by employing a Newtonian model for low shear stress. This bi-viscosity model ensures that the viscosity does not acquire extreme magnitude values for low shear stress regions, leading to numerical instabilities. Therefore, the fluid is assumed Newtonian with high viscosity for this critical region (Saliba, 2019). Consequently, the apparent viscosity $\nu_{0,m}$ represents the viscosity above which the fluid behaves like a solid. The initial estimate for $\nu_{0,m}$ is dependent on the material consistency K/ρ_m.

2.3.1 Flow parameters

Seeking reported events in the literature is essential to understanding the muddy flow behavior in an inclined plane. Through natural and measured flow mass movement events, appropriated scaled nature parameters are available, and with this, the comprehension of such phenomena becomes more tangible.

The study carried out by Berti *et al.* (2000), which discusses the event that took place in the Acquabona basin, Italy, provides the necessary input data parameters idea. Monitoring systems captured hydrological conditions, dynamic properties, and deposition processes favorable to debris flow occurrence. Among the most considerable measurements on August 17, 1998, the following were observed: precipitation rainfall totaling 29 millimeters, with 58 minutes duration; a

[1]Deviatoric Stress Tensor: difference between stress tensor and hydrostatic pressure tensor.

volume deposition range from 8000 to 9000 m^3; and flow velocities reaching up to 7.69 m/s. Ultrasonic sensors checked mass movements depths of 2 meters, approximately. Table 1 presents the simulation rheological parameters adopted based on the Acquabona event, rounding up some values for simplification, and the procedure described in section 2.2

Table 1: Mud rheological parameters adopted.

Parameter	Symbol	Value	Unit
Density	ρ_m	2000	kg/m^3
Flow index	n	0.30	[–]
Yield stress	τ_0	50	Pa
Fluid consistency	K	1000	1/Pa
Apparent viscosity	$\nu_{0,m}$	2	m^2/s

The dimensionless non-Newtonian fluid parameters are presented below. The flow Reynolds number, dimensionless that relates the inertial to the viscous forces, calculated according to Thompson and Soares (2016), is specified by Eq. (15):

$$Re_m = \frac{8\,\rho_m\,u_{0,m}^2}{\tau_0 + K\left(2\frac{u_{0,m}}{h_{0,m}}\right)^n} \tag{15}$$

where $h_{0,m} = 1$ m and $u_{0,m} = 3.14$ m/s, resulting in a dimensionless Reynolds number equivalent to $Re_m = 88$. Since $Re_m \ll 2000$, the flow is laminar.

The Froude number, also dimensionless, which indicates the kinetic energy relationship between horizontal and vertical forces, is as shown in Eq. (16):

$$Fr_m = \frac{u_{0,m}}{\sqrt{g\,h_{0,m}\cos\theta}} \tag{16}$$

Given that the slope of the channel is equal to $\theta = 7°$, the Froude number results in $Fr_m = 1$.

2.3.2 Meshing and Boundary conditions

Figure 3a shows the mesh used in the simulation. The parameter h_0 represents the general flow depth. When this parameter receives the fluid subscript (m for mud and N for Newtonian), it will correspond to the fluid respective flow depth. It can be seen that the domain is proportional to this parameter. The lower part of the mesh, which corresponds to the fluids region and the interface fluid-air, is more refined than the top. This configuration better captures the flow behavior in this region, which is more critical than the upper part of the domain, where just air is present. The solid fixed body geometry is emphasized by presenting H_{SB} and L_{SB}. Regarding both x and y-directions, the mesh is more refined according to its approximation of the obstacle. Figure 3b introduces the surfaces for boundary conditions implementation, which can be seen in Tab 2.

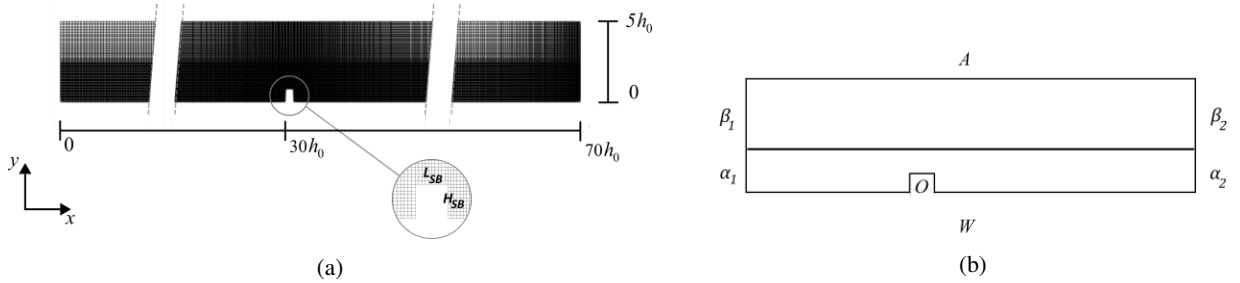

(a) (b)

Figure 3: Numerical configuration of the problem. (a) Mesh with the submerged solid body emphasized. (b) Surfaces for boundary condition settings, which can be seen in Tab. 2.

2.3.3 Mesh assessment

The grid convergence index is employed to quantitatively verify the mesh quality and guarantee the results independence of it. This part of the study evaluates the global variables of the problem, such as maximum velocity, mean pressure, and mean velocity. This assessment is verified at the obstacle x-position. Table 3 and Table 4. The grid convergence study

Table 2: Boundary conditions according with the geometric limits.

Surface	Geometric Limit	Boundary Condition		
		u_0 (m/s)	p (N/m^2)	α
α_1	$x = 0$, $y = [0; h_0]$, and $z = [0; h_0]$	$\frac{\partial u}{\partial n_F} = 0$	$\frac{\partial p}{\partial n_F} = 0$	1
α_2	$x = 70h_0$, $y = [0; h_0]$, and $z = [0; h_0]$	$\frac{\partial u}{\partial n_F} = 0$	$\frac{\partial p}{\partial n_F} = 0$	$\frac{\partial \alpha}{\partial n_F} = 0$
β_1	$x = 0$, $y = [2h_0; 5h_0]$, and $z = [0; h_0]$	$\frac{\partial u}{\partial n_F} = 0$	$\frac{\partial p}{\partial n_F} = 0$	0
β_2	$x = 70h_0$, $y = [2h_0; 5h_0]$, and $z = [0; h_0]$	$\frac{\partial u}{\partial n_F} = 0$	$\frac{\partial p}{\partial n_F} = 0$	$\frac{\partial \alpha}{\partial n_F} = 0$
A	$x = [0; 70h_0]$, $y = 5h_0$, and $z = [0; h_0]$	*	**	***
W	$x = [0; 30h_0] \cup [30h_0 + L_{SB}; 70h_0]$, $y = 0$, and $z = [0; h_0]$	0	$\frac{\partial p}{\partial n_F} = 0$	$\frac{\partial \alpha}{\partial n_F} = 0$
O	$x = [30h_0; 30h_0 + L_{SB}]$, $y = [0; H_{SB}]$, and $z = [0; h_0]$	0	$\frac{\partial p}{\partial n_F} = 0$	$\frac{\partial \alpha}{\partial n_F} = 0$

*, ** ,***: A zero-gradient condition is applied for outflow (as defined by the flux)
and for inflow, the velocity is obtained from the flux with the specified inlet direction

provides expected and satisfactory results since, for the three global variables, χ is approximately 1. The mesh M_1 among the two other meshes is the one that produces better results when comparing it with Richardson extrapolation (f_R).

Table 3: Objective parameters as a function of the corresponding numerical mesh.

Mesh	Cells	$\bar{u}_m$ [m/s]	$u_{m,max}$ [m/s]	$\bar{p}_m$ [kPa]	Computational time [s]
M_1	40000	3.1290	3.8487	9.7573	2200
M_2	10000	3.1234	3.8587	9.7761	397
M_3	2500	3.1593	3.9795	9.8518	111

Table 4: Mesh independence parameters calculated according to Roache (1994).

Roache parameter	$\bar{u}_m$	$u_{m,max}$	$\bar{p}_m$
GCI_{12}	4.1453×10^{-4}	2.9489×10^{-4}	7.9284×10^{-4}
GCI_{23}	0.0027	0.0035	0.0032
f_R	3.1301 m/s	3.8478 m/s	9.7511 kPa
χ	0.9981	0.9974	1.0018

2.4 Newtonian equivalency procedure

The procedure of establishing an equivalent Newtonian fluid to compare with the non-Newtonian one is described in Fig. 4. Since $\tau_0 = 50$ Pa, $h_{0,m} = 1$ m, $u_{0,m} = 3.14$ m/s, and $n = 0.3$, the Newtonian dynamic viscosity results in $\mu = 464.82$ Pa·s. The density is considered the same for both fluids, that is $\rho_m = \rho_N$. Both fluid Froude numbers, shear stresses, and shear rates are considered equal to establish the kinematic equivalency. Since the Newtonian fluid mean velocity is unknown, it should be evaluated employing the flow rate. This last formulation provides a flow depth of $h_{0,N} \approx 1.50$ m, which gives a mean velocity of $u_{0,N} \approx 3.80$ m/s.

The Newtonian fluid Reynolds number, considering the hydraulic diameter (Pritchard and Mitchell, 2015), is described by Eq. (17).

$$Re_N = 4\left(\frac{\rho_N u_{0,N} h_{0,N}}{\mu}\right) \tag{17}$$

Hence both fluid Reynolds number are equivalent in magnitude, $Re_m = 88$ and $Re_N = 96$, the dynamic equivalency is guaranteed.

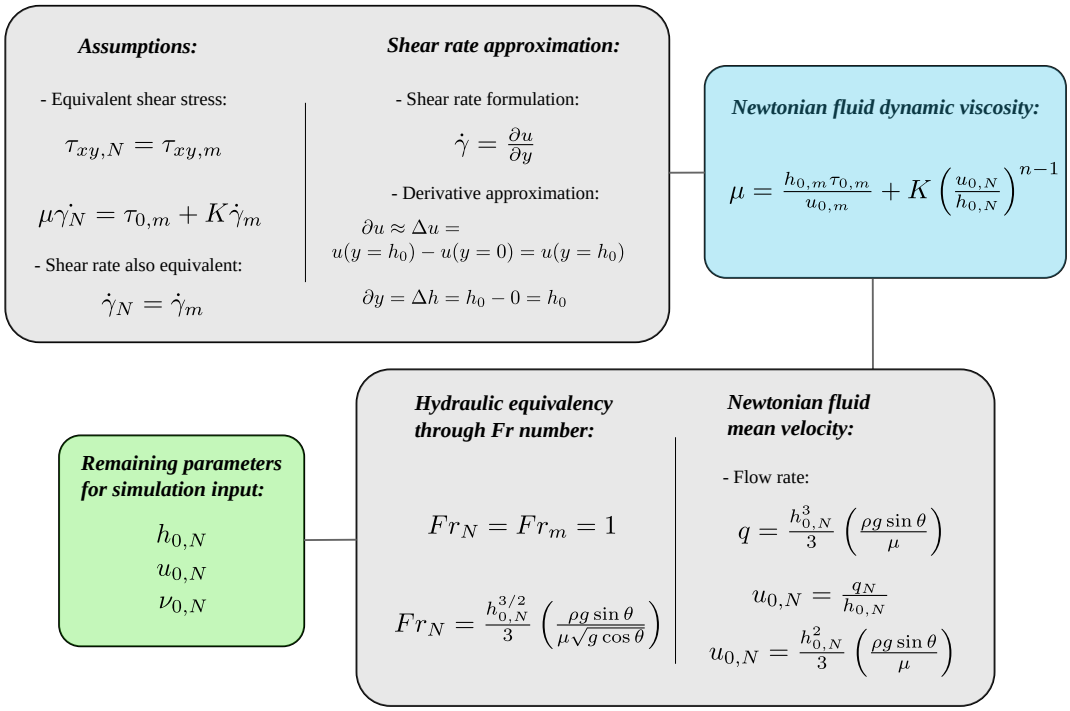

Figure 4: Diagram procedure for obtaining the Newtonian fluid simulation parameters.

3. RESULTS

This section presents the assessment of both mud and Newtonian fluids behavior. The dynamic and kinematic simulation results are presented, along with observations of the free surface level on the domain, according to the obstacle height H_{SB}. The red line and square marker correspond to the simulation results that employed the muddy fluid, while the blue line and circle marker, to the Newtonian one.

Figure 5 shows the simulation results for forces according to H_{SB} increasing values. For both Fig. 5a and Fig. 5b, which respectively show the pressures and viscous forces, the forces exerted by the Newtonian fluid on the fixed solid body are greater than those made by the muddy one. Pressure and viscous forces are H_{SB} and can be approximated by quadratic functions. The pressure forces, with concave curves up, present an inflection point for $H_{SB} \approx 0.3$ m in both curves showing the lowest pressure forces at this position. For $H_{SB} > 0.4$ m values, the pressure force tends to increase considerably, suggesting a proportionality to the quantity of fluid retained (a dam-like behavior). The viscous forces values have an asymptotic behavior when the obstacle height reaches $H_{SB} \approx 0.8$ m.

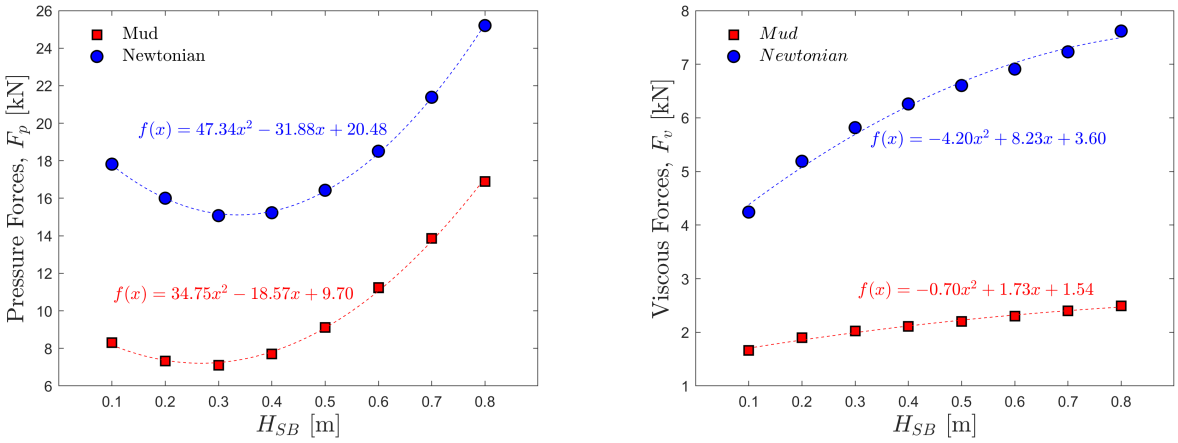

(a) Pressure forces.

(b) Viscous forces.

Figure 5: Forces results according with H_{SB} values.

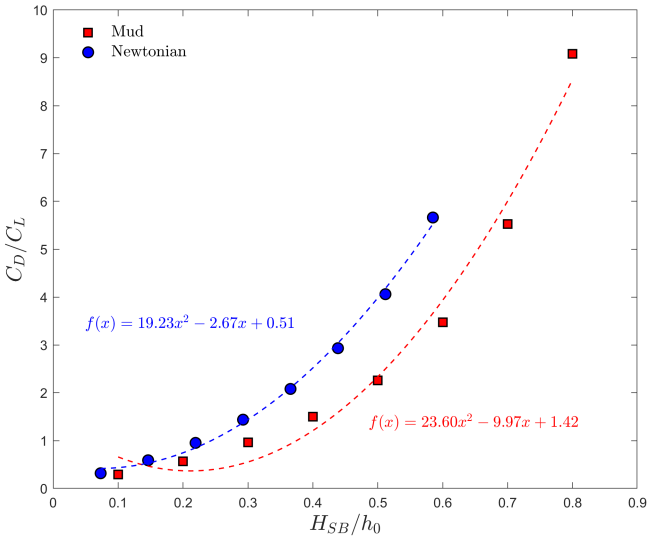

Figure 6: C_D/C_L ratio due to submergence ratio (H_{SB}/h_0).

Figure 6 presents the C_D/C_L ratio as a function of the submergence ratio (H_{SB}/h_0). These results consider that C_L is pointing downward, meaning that downforce is applied to the obstacle, pushing it against the channel bed. The submergence ratio indicates how much the solid body is submerged proportionally to the flow. It can be seen that for a given submergence ratio value, the Newtonian fluid flow presents greater C_D/C_L ratio values. Therefore, the Newtonian fluid could drag an obstacle with more capacity than the non-Newtonian one. This condition tends to increase with higher values of the submergence ratio. One critical point could be assumed when $C_D/C_L > 1$, meaning that the downforce would be smaller than the drag force, effectively changing the inertial condition of the obstacle. The effective dragging of the body would happen within this range – without considering its weight and friction with the channel bed. This observation can be verified at lower values of H_{SB}/h_0 for the Newtonian fluid, as presented in Fig. 6.

Figure 7 shows the free surface height in accord with H_{SB} proximity. H is the quotient between the y-axis and the h_0 correspondent fluid, and X is the quotient between the x-axis and h_0. $X = 0$ is the origin of the x^*-axis, denoting the positioning placement of the obstacle. It can be seen, through qualitative analysis, that the flow significantly varies

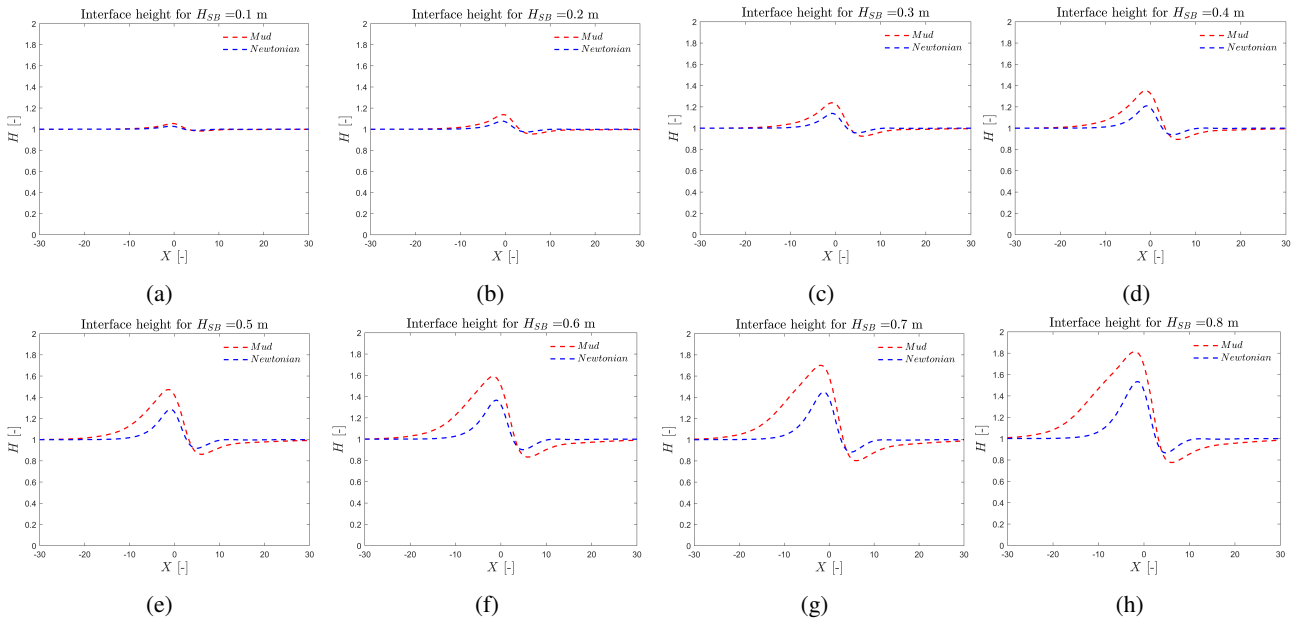

Figure 7: Interface due to the obstacle height.

the free surface height near the solid body when H_{SB} increases. The general scenario shows that the solid body imposes an increase in the free surface height upstream of the submerged body and a decrease downstream of the body. As H_{SB}

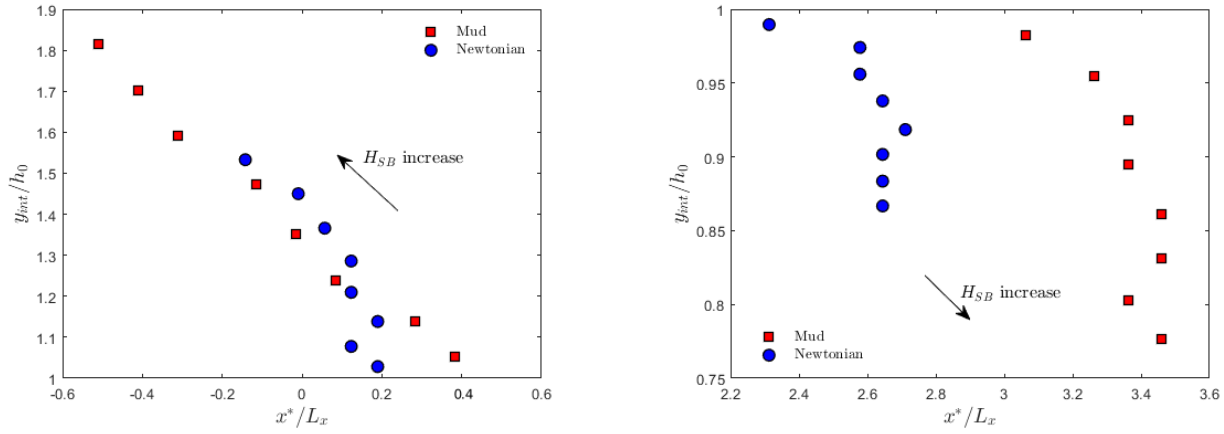

(a) (b)

Figure 8: Interface maximum and minimum values.

increases, the upstream flow height increases, and the downstream flow height decreases. Although the general behavior for both fluid flows is similar, some discrepancies in the free surface variation and its geometrical shape around the submerged body are perceived. Therefore, both potential and kinetic energies are expected to have different influences on the submerged body dynamic behavior, as shown by the previous discussion, when considering C_D/C_L. Also, from the results shown in Fig. 7 one would expect that the non-Newtonian fluid flow would promote a higher angular momentum than the equivalent Newtonian fluid.

To explore what happens with the interface close to the submerged body in detail, Fig. 8 shows the interface maximum and minimum values. Both axes are dimensionless, where the vertical axis is the position of the free surface height (maximum or minimum) divided by the respective mean flow height h_0, and the horizontal auxiliary axis x^* is divided by the length of each simulation domain. Figure 8a shows that higher values for the upstream flow height follow the H_{SB} increase and tend to move away from the submerged body. The non-Newtonian fluid presents higher range values in both the x and y domain directions. It is essential to see that for the first two values of H_{SB}, that is 0.1 and 0.2 m, the Newtonian maximum height interface starts to grow beforehand comparing to mud. However, for $H_{SB} = 0.3$ m, the non-Newtonian height interface surpasses this behavior, and the difference between their values becomes higher. Figure 8b shows that for the Newtonian fluid flow, the minimum free surface height appears closer to the fixed solid body for $x^*/L_x < 2.8$, while the non-Newtonian free surface draws away downstream from the submerged body, reaching $x^*/L_x \sim 3.4$. Both Fig. 8a and Fig. 8b show that the results are not monotonic and vary slightly depending on the simulation – result from the interpolation used in post-processing.

4. CONCLUSION

The study concerns a free-surface flow over an inclined slope, where specific climate and soil conditions can lead to mass movements. Depending on the magnitude of the forces exerted on a given obstacle by the flow, this body can be dragged and potentially increase the damage to vulnerable regions.

The simulation, therefore, tried to reproduce this event in a steady-state condition to understand this type of flow and its environmental consequences through a fundamental and simplified approach. Additionally, simulations using two different fluids, a non-Newtonian and a Newtonian, were made to perceive how important it would be to use the proper rheological model. To compare both fluids simulations, a procedure of searching the fluid parameters that would establish equivalency with a Newtonian fluid was conducted – aiming at dynamic and kinematic proportions.

After this procedure, the simulation results were evaluated for both fluids and showed that the pressure and viscous forces and the C_D/C_L ratio are H_{SB} functions. Also, the submergence ratio can provide insights into the flow magnitude and capacity. Results showed that the Newtonian fluid would have higher efficiency for transporting/carrying an obstacle than the non-Newtonian one. This condition tends to increase along with the obstacle submergence ratio higher values. On the other hand, the free-surface flow height can measure how both fluid flows are affected by the submerged solid body presence. The non-Newtonian fluid presented the widest free-surface variation ranges. The maximum and minimum flow height – reaching higher and more distant values for maximum values and lower and more distant values of the minimum free-surface interface – suggest that the non-Newtonian fluid flow could have more capacity to overturn an object.

5. REFERENCES

Ancey, C., 2007. "Plasticity and geophysical flows: A review". *Journal of Non-Newtonian Fluid Mechanics*, Vol. 142, No. 1-3, pp. 4–35. ISSN 03770257. doi:10.1016/j.jnnfm.2006.05.005.

Berti, M., Genevois, R., LaHusen, R., Simoni, A. and Tecca, P.R., 2000. "Debris flow monitoring in the Acquabona watershed on the Dolomites (Italian Alps)". *Physics and Chemistry of the Earth, Part B: Hydrology, Oceans and Atmosphere*, Vol. 25, No. 9, pp. 707–715. ISSN 14641909. doi:10.1016/S1464-1909(00)00090-3.

Berti, M., Genevois, R., Simoni, A. and Tecca, P.R., 1999. "Field observations of a debris flow event in the Dolomites". *Geomorphology*, Vol. 29, No. 3-4, pp. 265–274. ISSN 0169555X. doi:10.1016/S0169-555X(99)00018-5.

Cabral, V.C., Reis, F.A.G.V., D'Affonseca, F.M., Lucía, A., dos Santos Corrêa, C.V., Veloso, V., Gramani, M.F., Ogura, A.T., Lazaretti, A.F., Vemado, F., Pereira Filho, A.J., dos Santos, C.C., Lopes, E.S.S., Rabaco, L.M.R., do Carmo Giordano, L. and Zarfl, C., 2021. "Characterization of a landslide-triggered debris flow at a rainforest-covered mountain region in Brazil". *Natural Hazards*, Vol. 108, No. 3, pp. 3021–3043. ISSN 15730840. doi:10.1007/s11069-021-04811-9.

Chen, M., Tang, C., Zhang, X., Xiong, J., Chang, M., Shi, Q., Wang, F. and Li, M., 2021. "Quantitative assessment of physical fragility of buildings to the debris flow on 20 August 2019 in the Cutou gully, Wenchuan, southwestern China". *Engineering Geology*, Vol. 293, No. October 2020, p. 106319. ISSN 00137952. doi:10.1016/j.enggeo.2021.106319.

Coussot, P. and Meunier, M., 1996. "Recognition, classification and mechanical description of debris flows". *Earth-Science Reviews*, Vol. 40, No. 3-4, pp. 209–227. ISSN 00128252. doi:10.1016/0012-8252(95)00065-8.

Fiorot, G.H. and Maciel, G.d.F., 2019. "Free-surface laminar flow of a Herschel–Bulkley fluid over an inclined porous bed". *Journal of Non-Newtonian Fluid Mechanics*, Vol. 272, No. April, p. 104164. ISSN 03770257. doi:10.1016/j.jnnfm.2019.104164.

Gramani, M.F. and Arduin, D.H., 2015. "Morfologia da drenagem e dos depósitos de debris flow em Itaóca, São Paulo". *15º Congresso Brasileiro de Geologia de Engenharia e Ambiental*, Vol. CBGE, No. 11, pp. 1–10.

Irgens, F., 2014. *Rheology and non-Newtonian Fluids*. Springer Netherlands, Trondheim, Norway. ISBN 9783319010526.

Kanji, M.A., Cruz, P.T. and Massad, F., 2008. "Debris flow affecting the Cubatão Oil Refinery, Brazil". *Landslides*, Vol. 5, No. 1, pp. 71–82. ISSN 1612-510X. doi:10.1007/s10346-007-0110-3.

Maciel, G.d.F., Dos Santos, H.K. and Ferreira, F.d.O., 2009. "Rheological analysis of water clay compositions in order to investigate mudflows developing in canals". *Journal of the Brazilian Society of Mechanical Sciences and Engineering*, Vol. 31, No. 1, pp. 64–74. ISSN 16785878.

Malet, J.P., Remaître, A., Maquaire, O., Ancey, C. and Local, J., 2003. "Flow susceptibility of heterogeneous marly formations: Implications for torrent hazard control in the Barcelonnette Basin (Alpes-de-Haute-Provence, France)". *International Conference on Debris-Flow Hazards Mitigation: Mechanics, Prediction, and Assessment, Proceedings*, Vol. 1, No. January, pp. 351–362.

Mueting, A., Bookhagen, B. and Strecker, M.R., 2021. "Identification of Debris-Flow Channels Using High-Resolution Topographic Data: A Case Study in the Quebrada del Toro, NW Argentina". doi:10.1029/2021JF006330.

Nguyen, V.H., Rémond, S., Gallias, J.L., Bigas, J.P. and Muller, P., 2006. "Flow of Herschel-Bulkley fluids through the Marsh cone". *Journal of Non-Newtonian Fluid Mechanics*, Vol. 139, No. 1-2, pp. 128–134. ISSN 03770257. doi:10.1016/j.jnnfm.2006.07.009.

OpenFOAM UserGuide, O., 2020. *OpenFOAM User Guide version 8*. July. The OpenFOAM Foundation.

Picanço, J., Vieira, B., Martins, T., Gramani, M., Faccuri, G. and Silva, M., 2019. "Debris-flow occurrence in granite landscape in south-southeast Brazil". *Debris-Flow Hazards Mitigation: Mechanics, Monitoring, Modeling, and Assessment - Proceedings of the 7th International Conference on Debris-Flow Hazards Mitigation*, pp. 798–807.

Pritchard, P.J. and Mitchell, J.W., 2015. *Fox and McDonald's introduction to fluid mechanics*. John Wiley & Sons. ISBN 978-1-118-91265-2.

Roache, P.J., 1994. "Perspective: A Method for Uniform Reporting of Grid Refinement Studies".

Saliba, J., 2019. *Optimisation of Flow Distribution for Pipe Pullback in Horizontal Directional Drilling*. Ph.D. thesis, Delft University of Technology.

Thompson, R.L. and Soares, E.J., 2016. "Viscoplastic dimensionless numbers". *Journal of Non-Newtonian Fluid Mechanics*, Vol. 238, No. December, pp. 57–64. ISSN 03770257. doi:10.1016/j.jnnfm.2016.05.001.

6. RESPONSIBILITY NOTICE

The authors are solely responsible for the printed material included in this paper.